Supporting Information (SI) Appendix
Laser-Induced Transient Magnons in $Sr_3Ir_2O_7$ Throughout the Brillouin Zone

I. SI TIME-RESOLVED RESONANT ELASTIC X-RAY SCATTERING RESULTS

The response of magnetic long-range order on the laser pump was first investigated via reciprocal lattice scans along the $(0, 0, L)$ and $(H, 0, 0)$ directions around the (-3.5, 1.5, 18) magnetic Bragg peak [notation in reciprocal lattice units (r.l.u)]. Figure S1 displays datasets before and ~2.5 ps after the arrival of a 32.2 mJ/cm^2 strong laser pulse. The laser radiation induces a suppression, but no broadening, of the magnetic Bragg peak within our experimental Q-resolution. This provides evidence that all crucial information on transient magnetic long-range order is captured by the evolution of the magnetic Bragg peak intensity. It is noted that additional H- and L-scans were taken ~40 ps after laser excitation confirming this conclusion.
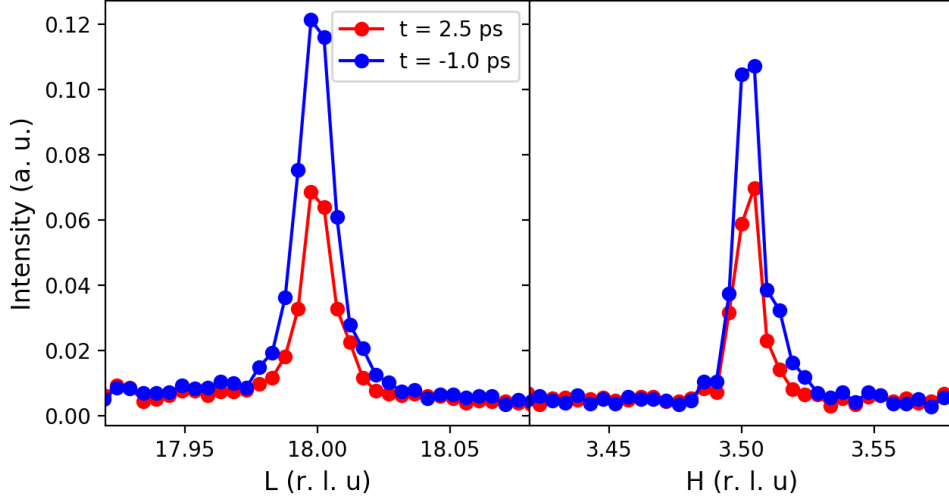
FIG. S1. Laser effect on the magnetic Bragg peak. Reciprocal lattice scans along $(0, 0, L)$ and $(H, 0, 0)$ around (-3.5, 1.5, 18) magnetic Bragg peak in reciprocal lattice units (r.l.u). The blue color denotes a scan that was taken before, and the red dataset ~2.5 ps after the arrival of a 32.2 mJ/cm^2 strong laser pulse. Only a suppression of the Bragg peak is observed.

Figure S2A shows the (-3.5, 1.5, 18) magnetic Bragg signal on the area detector before and around 1 ps after the arrival of the laser pulse. The time evolution of the depleted magnetic Bragg peak intensity is shown in the upper panel of Fig. S2B. Immediately after the optical pump ($t = 0$) magnetism is reduced by 50-75% for laser fluences between 5.2 and 32.2 mJ/cm^2. A significant fraction of the magnetic signal is recovered within the first picoseconds, but a slower process is superimposed preventing the full restoration of the original magnetic state. As a result, the reduced magnetic peak intensity stays roughly constant in the range between 5 and 500 ps without noticeable recovery. Furthermore, it is noted that a faint oscillatory behavior appears ~50 ps after laser impact for fluences larger than 14.2 mJ/cm^2. This feature is a typical signature of a strain wave that is propagating through the crystal and subsequently reflected at the sample boundary [1–3].

The time evolution of the transient magnetic long-range order is described by the minimal phenomenological model

$$I(t) = \begin{cases} 1 - Ae^{-t/\tau_{\text{mag}}} - C(1 - e^{-t/\tau_{\text{mag}}}) + De^{-t/\tau_{\text{wave}}} \sin(\omega t), & \text{for } t \geq 0 \\ 1, & \text{for } t < 0 \end{cases}, \tag{1}$$

where A quantifies a prompt, step-like decay at $t = 0$ (as it is much faster than the time resolution), which recovers on a timescale τ_{mag}, and C is the fraction of the order that has not been restored in 500 ps. The strain wave features an amplitude D, decay time τ_{wave} and oscillation frequency ω. The measured magnetic Bragg peak intensity is modeled by convolving $I(t)$ with a Gaussian function in order to account for our finite time resolution of 0.15 ps (full-width at half-maximum). The initial decay of magnetic long-range order was found to be much faster than the time resolution, and was thus approximated as an instantaneous step function in Eq. 1.

Robust fits of experimental results were obtained by constraining the amplitude of the strain wave to $D = 0.5$. The frequency of the strain wave at 23.3 mJ/cm^2 was fixed to 0.03 rad/s (the mean value of all other conditions) to
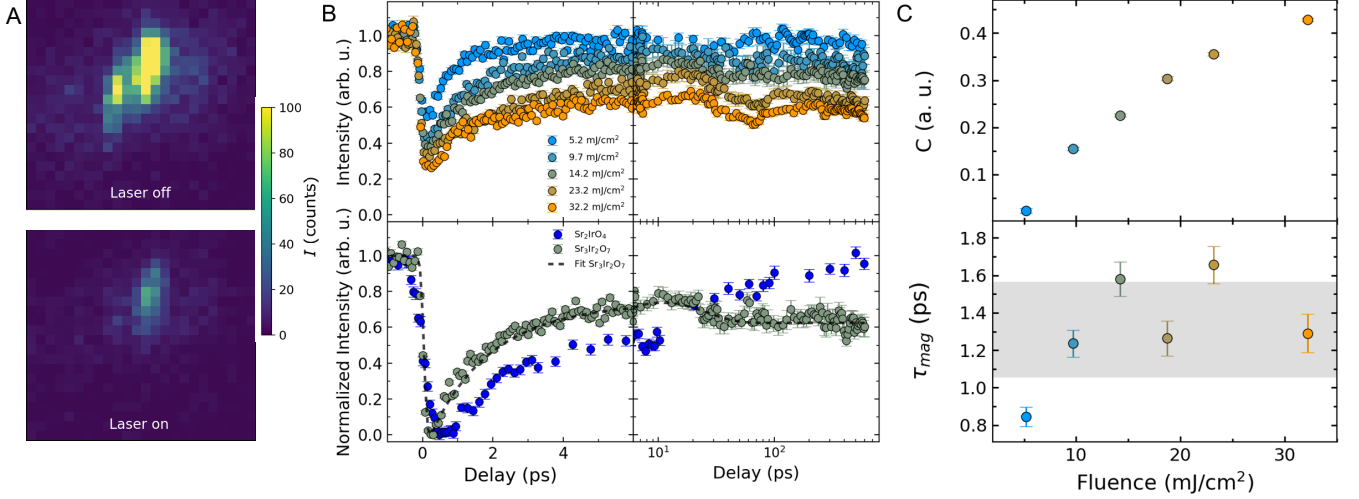
FIG. S2. Time evolution of magnetic order in $Sr_3Ir_2O_7$. (A) Intensity of the (-3.5, 1.5, 18) magnetic Bragg peak [notation in reciprocal lattice units (r.l.u)] in equilibrium (top) and after laser radiation of ∼20 mJ/cm^2 (bottom). The detector pixels are 0.0086 r.l.u wide (B) Top panel: Relative magnetic Bragg peak intensity as a function of time delay. The error bars follow Poissonian statistics. Panel is split into short (6 ps) and long (100 ps) time ranges for clarity. Bottom panel: 14.2 mJ/cm^2 $Sr_3Ir_2O_7$ data normalized to the maximal depleted volume fraction and fit with the model shown in Eq. 1. The results are compared to data for Sr_2IrO_4 taken from Ref. [4] with a fluence chosen to match the fast recovery of the magnetic volume fraction. Heisenberg-like Sr_2IrO_4 reveals a slow recovery with onset around 100 ps, which is absent in gapped $Sr_3Ir_2O_7$. (C) Fluence dependence of the persistent transient fraction, C, and the fast recovery timescale τ_{mag}. The gray area shows the standard deviation around the statistical mean value of the fast recovery timescale, $i.e.$ $\tau_{mag} = 1.3(3)$ ps.

further stabilize the fit. All other parameters were varied freely and shown in Tab. 1. It is noted that even for strong fluences $A < 1$, suggesting some experimental mismatch between pumped laser and probed x-ray volumes (see also below). This emphasizes the need to also include contributions like the energy transfer out of the illuminated sample volume in theoretical approaches that model transient magnetic states.

The lower panel of Fig. S2B displays the best fit to the normalized intensity at 14.2 mJ/cm^2 (see also Materials and Methods section). The fluence dependence of τ_{mag} and C is displayed in Fig. S2C. The fast timescale $\tau_{mag} = 1.3(3)$ ps is fluence independent and we find $C > 0$ for all fluences. This is different than in nearly gapless Sr_2IrO_4 - a related material where at fluences leading to a similar fast recovery of the magnetic volume fraction, the onset of a slow magnetic recovery is observed around 100 ps (see lower panel of Fig. S2B) [4]. The different behaviors are likely to arise from their distinct magnetic interactions and resulting magnon dispersions. A phonon-assisted energy transfer from excited (pseudo-)spins into the lattice degrees of freedom, for instance, is expected to be reduced in large gap antiferromagnets, yielding a much slower magnetic recovery when compared to nearly gapless materials.

TABLE I. Time evolution of REXS fitting parameters. Time dependence of the depleted magnetic volume fraction A, the unrecovered volume C after 500 ps, the fast recovery timescale τ_{mag} and the timescale τ_{wave} and frequency ω of the strain wave.

fluence (mJ/cm^2)	A	C	τ_{mag} (ps)	τ_{wave} (ps)	ω (rad/s)
5.2	0.54(4)	0.023(5)	0.85(5)	NaN	NaN
9.7	0.66(3)	0.154(4)	1.24(7)	12(2)	0.025(4)
14.2	0.65(2)	0.225(3)	1.58(9)	11(1)	0.035(4)
18.7	0.72(4)	0.303(4)	1.26(9)	18(2)	0.027(3)
23.2	0.71(2)	0.356(4)	1.7(1)	19(1)	0.03 (fixed)
32.2	0.78(2)	0.429(4)	1.3(1)	13(1)	0.033(4)
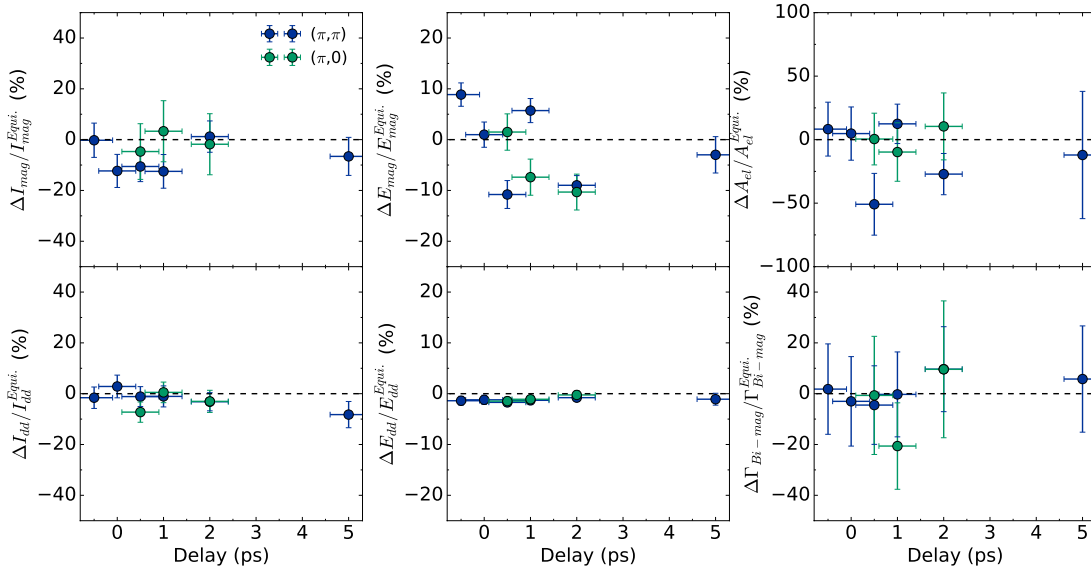
FIG. S3. Time evolution of RIXS fitting parameters. Relative time dependence of the integrated magnon, I_{mag}, and orbital, I_{dd}, intensity, the magnon and orbital position, E_{mag} and E_{dd}, the amplitude of the elastic line, A_{el}, and the full-width at half-maximum of the broad magnetic feature $\Gamma_{\mathrm{Bi\text{-}mag}}$ at higher energies.

II.   SI TIME-RESOLVED RESONANT INELASTIC X-RAY SCATTERING RESULTS

The time-resolved resonant inelastic x-ray scattering (tr-RIXS) spectra in Fig. 2a and b of the main manuscript reveal an elastic line, a collective magnon at $\sim$100 and 150 meV for (π, π) and $(\pi, 0)$, respectively, a magnon continuum at $\sim$250 meV and an orbital excitation at 680 meV. A sum of four Gaussian-shaped peaks was used to represent the energy-loss data. The center of the elastic line and its width were fixed in the analysis to 0 meV and the experimental resolution of 70 meV, respectively. Robust fits were obtained by further constraining the energy of the magnon continuum to 260 meV and its amplitude to the mean free value of 2.02 and 1.44 for (π, π) and $(\pi, 0)$, respectively. All other parameters were varied freely. Figure S3 shows the relative time dependence of the integrated magnon, I_{mag}, and orbital, I_{dd}, intensity, the magnon and orbital position, E_{mag} and E_{dd}, the amplitude of the elastic line, A_{el}, and the width of the broad magnon feature $\Gamma_{\mathrm{Bi\text{-}mag}}$. Significant changes are observed only in the amplitude and width of the magnon and orbital excitation that are discussed in the main manuscript.

III.   SI ESTIMATION OF THE X-RAY AND LASER PENETRATION DEPTH

The optical penetration depth Λ of a beam incident at angle α with respect to the sample surface is defined by [5]

$$\Lambda = \frac{\lambda}{4\pi} \left[\Im \left(\sqrt{\tilde{N}^2 - \cos^2(\alpha)} \right) \right]^{-1}, \tag{2}$$

where $\Im$ signifies the imaginary part, λ is radiation wavelength, and $\tilde{N} = n + ik$ is the complex index of refraction. We define the penetration depth as the distance over which the beam intensity drops by $1/e$, and we remind the reader that $\tilde{N} = \sqrt{\tilde{\varepsilon}}$ where $\tilde{\varepsilon}$ is the relative permittivity. For the x-ray calculation, the dielectric constants below and above the Ir L-edge were calculated based on the crystal structure of $\mathrm{Sr_3Ir_2O_7}$ using the xrayutilities Python package [6]. The imaginary part of the index of refraction at the resonance was corrected considering the x-ray absorption white-line intensity [7]. At the Ir L_3-edge we find $\Lambda_{\mathrm{x\text{-}ray}} = 162$, 214 and 378 nm for $\alpha = 1.6, 2.1$ and $3.7°$, respectively. Using the reported optical conductivity results of Ref. [8], we find $\Lambda_{\mathrm{laser}} \approx 82$ nm for $\alpha \approx 20°$.

IV. SI SPIN-WAVE DISPERSION AND ESTIMATION OF NÉEL TEMPERATURE

The superexchange interactions in octahedrally coordinated $5d^5$ iridates are strongly dependent on bond angles. In general, isotropic Heisenberg, anisotropic Heisenberg, Dzyaloshinskii-Moriya and Kitaev exchange couplings can be present. For the simplified case of exactly straight bonds, symmetric octahedra coordination and assuming that Coulomb repulsion, U, is much larger than Hund's exchange, J_H, pseudo-dipolar and Kitaev interactions vanish by symmetry and the magnetic exchange becomes purely isotropic Heisenberg-like [9]. Since Sr_2IrO_4 and $Sr_3Ir_2O_7$ possess iridium-oxygen-iridium bond angles that are close to $180°$ [10–12], the dominant exchange term is Heisenberg-like, and the subdominant terms are anisotropic Heisenberg, Dzyaloshinskii-Moriya and Kitaev exchanges with the latter term generally considered negligible. This has been predicted in several theoretical works [13–15] and verified by RIXS and Raman scattering [16–18]. Thus, magnetism in Sr_2IrO_4 can be described by a Heisenberg Hamiltonian with in-plane isotropic coupling J, anisotropic coupling Γ, Dzyaloshinskii-Moriya interaction D and interlayer coupling J_c [13]

$$H_{214} = \sum_{\langle \vec{n}, \vec{m} \rangle} \left[J \vec{S}_{\vec{n}} \vec{S}_{\vec{m}} + \Gamma S_{\vec{n}}^z S_{\vec{m}}^z + D(-1)^{n_x + n_y}(S_{\vec{n}}^x S_{\vec{m}}^y - S_{\vec{n}}^y S_{\vec{m}}^x) \right] + \sum_{\langle\langle \vec{n}, \vec{m} \rangle\rangle} J_2 \vec{S}_{\vec{n}} \vec{S}_{\vec{m}} + \sum_{\langle\langle\langle \vec{n}, \vec{m} \rangle\rangle\rangle} J_3 \vec{S}_{\vec{n}} \vec{S}_{\vec{m}} + \sum_{\vec{n}, l} J_c \vec{S}_{\vec{n}, l} \vec{S}_{\vec{n}, l+1}.$$
(3)

Here, $\vec{n} = (n_x, n_y)$ are vectors to sites within the IrO_2 layers and l is the layer index, defining $\vec{S}_{\vec{n}, l}$ as the spin operator at site $\vec{n}$ of layer l. $\langle \vec{n}, \vec{m} \rangle$, $\langle\langle \vec{n}, \vec{m} \rangle\rangle$ and $\langle\langle\langle \vec{n}, \vec{m} \rangle\rangle\rangle$ denote first, second and third nearest neighbors in the tetragonal plane and J, J_2 and J_3 are the corresponding isotropic interaction constants. We mention that some reported models also include an anisotropic, symmetric exchange term in H_{214} [14, 15]. This term is, however, much smaller than the interlayer coupling and can, thus, be neglected for our purposes.

In cases where the spins are aligned in the tetragonal plane, the nearest-neighbor interactions in Eq. 3 can be mapped onto an effective isotropic exchange Hamiltonian with interlayer coupling as [13]:

$$H_{\text{iso}} = \sum_{\langle \vec{n}, \vec{m} \rangle} \tilde{J} \vec{\tilde{S}}_{\vec{n}} \vec{\tilde{S}}_{\vec{m}} + \sum_{\vec{n}, l} J_c \vec{\tilde{S}}_{\vec{n}, l} \vec{\tilde{S}}_{\vec{n}, l+1}.$$
(4)

The transformation involves a rotation of the two sublattices in the tetragonal plane, where $\vec{\tilde{S}}_{\vec{n}, l}$ is the rotated spin operator and $\tilde{J} = \sqrt{J^2 + D^2}$. Since the transition temperature in the case of $J \gg J_c$ is dominated by the spin-wave velocity, we have neglected the second and third nearest neighbor couplings here. T_N is defined as the temperature for which the expectation value $\langle \bar{S}_{\vec{n}}^x \rangle$ (calculated with linear spin-wave theory) vanishes. For $T_N \ll J/2$ the Néel temperature is given by [19]

$$T_N = \frac{\pi \tilde{J}}{\log\left(\frac{T_N^2}{4 \tilde{J} J_c}\right)}.$$
(5)

So if the interlayer coupling in Sr_2IrO_4 could be switched off, it would be predicted not to display magnetic order at any finite temperature. Using $\tilde{J} = 50$ meV to match a spin-wave energy of 200 meV at $(\pi, 0)$, we can reproduce the experimentally observed $T_N = 285$ K by assuming an interlayer coupling of 1.1 μeV. $T_N = 384.2$ K is obtained when using the previously reported value $J_c = 15.9$ μeV [13].

As c-axis couplings gain particular importance in $Sr_3Ir_2O_7$ the Hamiltonian of Eq. 3 needs to be extended to

$$H_{327} = \sum_{\langle \vec{n}, \vec{m} \rangle, l} \left[J \vec{S}_{\vec{n}, l} \vec{S}_{\vec{m}, l} + \Gamma S_{\vec{n}, l}^z S_{\vec{m}, l}^z \right] + \sum_{\langle \vec{n}, \vec{m} \rangle, l} D(-1)^{n_x + n_y + l}(S_{\vec{n}, l}^x S_{\vec{m}, l}^y - S_{\vec{n}, l}^y S_{\vec{m}, l}^x)$$
$$\sum_{\vec{n}} \left[J_c \vec{S}_{\vec{n}, 1} \vec{S}_{\vec{n}, 2} + \Gamma_c S_{\vec{n}, 1}^z S_{\vec{n}, 2}^z \right] + \sum_{\vec{n}} D_c (-1)^{n_x + n_y}(S_{\vec{n}, 1}^x S_{\vec{n}, 2}^y - S_{\vec{n}, 1}^y S_{\vec{n}, 2}^x)$$
(6)

with the additional terms Γ_c and D_c, which couple the planes within a bilayer. This model neglects coupling between the bilayers. The Néel temperature of a collinear antiferromagnetic spin alignment is found from the numerical solution of $\langle S_{\vec{n}, l}^z \rangle = 0$ with

$$\langle S_{\vec{n}, 1}^z \rangle = 1 - \frac{1}{16\pi^2} \int \left[\frac{B_{\vec{q}, +}}{E_+(\vec{q})} \coth\left(\beta E_+(\vec{q})\right) + \frac{B_{\vec{q}, -}}{E_-(\vec{q})} \coth\left(\beta E_-(\vec{q})\right) \right] \mathrm{dq_x dq_y}.$$
(7)

$E_\pm(\vec{q}) = \sqrt{B_{\vec{q},\pm}^2 - |C_{\vec{q},\pm}|^2}$ define the two magnon branches with

$$\beta = 1/(k_\mathrm{B} T_N)$$
$$B_{\vec{q},\pm} = \frac{1}{2}(8J + 8\Gamma + J_c + \Gamma_c) - 4J_2(1 - \cos(q_x)\cos(q_y)) - 4J_3(1 - \gamma_{2\vec{q}}) - 2J_{2c}(1 \mp \gamma_{\vec{q}})$$
$$C_{\vec{q},\pm} = \frac{1}{2}(8J\gamma_{\vec{q}} \pm J_c) - \frac{i}{2}(8D\gamma_{\vec{q}} \pm D_c)$$
$$\gamma_{\vec{q}} = \frac{1}{2}(\cos(q_x) + \cos(q_y))$$

and $k_\mathrm{B} = 8.617 \cdot 10^{-2}$ meV/K the Boltzmann constant. A reasonable Néel temperature $T_\mathrm{N} = 118$ K, which is within a factor of three of the experimental value, is obtained for $J = 46.6$ meV, $J_\mathrm{c} = 25.2$ meV, $J_2 = 5.95$ meV, $J_3 = 7.3$ meV, $J_\mathrm{2c} = 6.2$ meV, $\Gamma = 2.2$ meV, $\Gamma_\mathrm{c} = 34.3$ meV, $D = 12.25$ meV and $D_\mathrm{c} = 28.1$ meV. The analysis shows that magnetic order perpendicular to the tetragonal plane can be stabilized even in the absence of long-range c-axis coupling. Furthermore, in $Sr_3Ir_2O_7$ we do not expect the same extreme anisotropy between the ab-plane and c-axis correlations as in Sr_2IrO_4.

---

[1] H. J. Zeiger, J. Vidal, T. K. Cheng, E. P. Ippen, G. Dresselhaus, and M. S. Dresselhaus, Theory for displacive excitation of coherent phonons, Phys. Rev. B **45**, 768 (1992).

[2] A. Feist, N. Rubiano da Silva, W. Liang, C. Ropers, and S. Schäfer, Nanoscale diffractive probing of strain dynamics in ultrafast transmission electron microscopy, Structural Dynamics **5**, 014302 (2018).

[3] M. Lejman, G. Vaudel, I. C. Infante, P. Gemeiner, V. E. Gusev, B. Dkhil, and P. Ruello, Giant ultrafast photo-induced shear strain in ferroelectric $BiFeO_3$, Nature communications **5**, 4301 (2014).

[4] M. P. M. Dean, Y. Cao, X. Liu, S. Wall, D. Zhu, R. Mankowsky, V. Thampy, X. M. Chen, J. G. Vale, D. Casa, J. Kim, A. H. Said, P. Juhas, R. Alonso-Mori, J. M. Glownia, A. Robert, J. Robinson, M. Sikorski, S. Song, M. Kozina, H. Lemke, L. Patthey, S. Owada, T. Katayama, M. Yabashi, Y. Tanaka, T. Togashi, J. Liu, C. Rayan Serrao, B. J. Kim, L. Huber, C. L. Chang, D. F. McMorrow, M. Först, and J. P. Hill, Ultrafast energy- and momentum-resolved dynamics of magnetic correlations in the photo-doped mott insulator Sr_2IrO_4, Nature Materials **15**, 601 (2016).

[5] S. J. Orfanidis, Electromagnetic waves and antennas (Rutgers University, 2016) Chap. Reflection and Transmission, pp. 153–186.

[6] D. Kriegner, E. Wintersberger, and J. Stangl, *xrayutilities*: a versatile tool for reciprocal space conversion of scattering data recorded with linear and area detectors, Journal of Applied Crystallography **46**, 1162 (2013).

[7] C. Donnerer, M. M. Sala, S. Pascarelli, A. D. Rosa, S. N. Andreev, V. V. Mazurenko, T. Irifune, E. C. Hunter, R. S. Perry, and D. F. McMorrow, High-pressure insulator-to-metal transition in $Sr_3Ir_2O_7$ studied by x-ray absorption spectroscopy, Phys. Rev. B **97**, 035106 (2018).

[8] G. Ahn, S. J. Song, T. Hogan, S. D. Wilson, and S. J. Moon, Infrared spectroscopic evidences of strong electronic correlations in $(Sr_{1-x}La_x)_3Ir_2O_7$, Scientific Reports **6**, 32632 (2016).

[9] G. Jackeli and G. Khaliullin, Mott insulators in the strong spin-orbit coupling limit: From Heisenberg to a quantum compass and Kitaev models, Phys. Rev. Lett. **102**, 017205 (2009).

[10] J. G. Rau, E. K.-H. Lee, and H.-Y. Kee, Spin-orbit physics giving rise to novel phases in correlated systems: Iridates and related materials, Annual Review of Condensed Matter Physics **7**, 195 (2016).

[11] C. Rayan Serrao, J. Liu, J. T. Heron, G. Singh-Bhalla, A. Yadav, S. J. Suresha, R. J. Paull, D. Yi, J.-H. Chu, M. Trassin, A. Vishwanath, E. Arenholz, C. Frontera, J. Železný, T. Jungwirth, X. Marti, and R. Ramesh, Epitaxy-distorted spin-orbit Mott insulator in Sr_2IrO_4 thin films, Phys. Rev. B **87**, 085121 (2013).

[12] T. Hogan, L. Bjaalie, L. Zhao, C. Belvin, X. Wang, C. G. Van de Walle, D. Hsieh, and S. D. Wilson, Structural investigation of the bilayer iridate $Sr_3Ir_2O_7$, Phys. Rev. B **93**, 134110 (2016).

[13] T. Takayama, A. Matsumoto, G. Jackeli, and H. Takagi, Model analysis of magnetic susceptibility of Sr_2IrO_4: A two-dimensional $J_{\mathrm{eff}} = \frac{1}{2}$ Heisenberg system with competing interlayer couplings, Phys. Rev. B **94**, 224420 (2016).

[14] H. Liu and G. Khaliullin, Pseudo-Jahn-Teller effect and magnetoelastic coupling in spin-orbit Mott insulators, Phys. Rev. Lett. **122**, 057203 (2019).

[15] J. Porras, J. Bertinshaw, H. Liu, G. Khaliullin, N. H. Sung, J.-W. Kim, S. Francoual, P. Steffens, G. Deng, M. M. Sala, A. Efimenko, A. Said, D. Casa, X. Huang, T. Gog, J. Kim, B. Keimer, and B. J. Kim, Pseudospin-lattice coupling in the spin-orbit Mott insulator Sr_2IrO_4, Phys. Rev. B **99**, 085125 (2019).

[16] J. Kim, D. Casa, M. H. Upton, T. Gog, Y.-J. Kim, J. F. Mitchell, M. van Veenendaal, M. Daghofer, J. van den Brink, G. Khaliullin, and B. J. Kim, Magnetic excitation spectra of Sr_2IrO_4: Probed by resonant inelastic x-ray scattering: Establishing links to cuprate superconductors, Phys. Rev. Lett. **108**, 177003 (2012).

[17] J. Kim, A. H. Said, D. Casa, M. H. Upton, T. Gog, M. Daghofer, G. Jackeli, J. van den Brink, G. Khaliullin, and B. J. Kim, Large spin-wave energy gap in the bilayer iridate $Sr_3Ir_2O_7$: Evidence for enhanced dipolar interactions near the Mott metal-insulator transition, Phys. Rev. Lett. **109**, 157402 (2012).

[18] H. Gretarsson, N. H. Sung, M. Höppner, B. J. Kim, B. Keimer, and M. Le Tacon, Two-magnon Raman scattering and pseudospin-lattice interactions in Sr_2IrO_4 and $Sr_3Ir_2O_7$, Phys. Rev. Lett. **116**, 136401 (2016).

[19] V. Y. Irkhin and A. A. Katanin, Critical behavior and the néel temperature of quantum quasi-two-dimensional heisenberg antiferromagnets, Phys. Rev. B **55**, 12318 (1997).